Pergamon

Int. J. Heat Mass Transfer. Vol. 38, No. 8, pp. 1427–1442, 1995

0017-9310/95 $9.50+0.00

0017-9310(94)00249-5

Analysis of the critical Weber number at the onset of liquid entrainment in capillary-driven heat pipes

B. H. KIM and G. P. PETERSON†

Department of Mechanical Engineering, Texas A&M University, College Station, TX 77843-3123, U.S.A.

(*Received* 4 *March* 1994 *and in final form* 27 *July* 1994)

Abstract—Entrainment phenomena in capillary-driven heat pipes were studied and both analytical and experimental approaches were utilized to identify and better understand the parameters that govern the entrainment of liquid in operating heat pipes. A heat pipe experiment was conducted using a high power heat pipe, designed to verify the existence of the various modes of entrainment and measure the corresponding entrainment limits. In addition, entrainment limit data were theoretically verified using a computer model designed to predict the maximum performance for the given operating conditions. Entrainment was detected by various methods and classified into representative types according to the relative position of the liquid interface to the wick structure and the operating conditions. Results of the experiment were compared with those obtained from previous investigations presented by Cotter, Tien and Chung and Prenger and Kemme. From the comparison of the critical Weber number or vapor velocity, the effectiveness of previous aerodynamic simulations was also examined.

INTRODUCTION

As the heat input increases, the vapor velocity in operating heat pipes becomes high enough to cause liquid droplets to be stripped or torn off the wavy liquid–vapor interface and entrained in the vapor flow [1, 2]. This entrainment of liquid droplets limits the axial heat transport and is referred to as the entrainment limit.

For two-phase annular flow, numerous studies have been presented to predict the onset of entrainment. In general, the analytical approaches were made based upon the Kelvin–Helmholtz (K–H) of Rayleigh–Taylor instability theories [3–5], and various semi-empirical criteria were proposed by incorporating the critical Weber number analysis or flooding correlations with the existing experimental data [6, 7]. However, the entrainment phenomenon in two-phase thermosyphons or heat pipes, especially the presence of entrainment in capillary-driven heat pipes, has not been studied extensively. Busse and Kemme [8] have even expressed doubts as to the possibility of entrainment in the capillary-driven heat pipes since wicking structures are likely to retard the growth of surface waves.

It is even more difficult to predict the entrainment limit in heat pipes operating at an arbitrary temperature since the limit involves both the dimensions of the heat pipe and thermal properties of the working fluid. However, when the wick is fully flooded with working fluid, the entrainment limit or critical heat transport can be estimated by utilizing the critical vapor velocities obtained not only from the instability criteria, but also the classical two-phase annular flow models mentioned above and performing an energy balance for the given thermal properties and geometry of the vapor flow. Several analytical or semi-empirical criteria have been proposed to predict entrainment from properly saturated wicks since Cotter [9] first introduced the instability concept for operating heat pipes. The most popular analytical scheme is the Weber number criterion [10], which was derived from the force balance on a single wick pore.

Although several analytical or semi-empirical criteria have been proposed to predict the entrainment limit in heat pipes, most of these models have not proven reliable. As noted by Peterson and Bage [2], the entrainment limit predicted from these models may vary by as much as a factor of 30. In addition, little experimental data are available to justify the validity for different wick geometries and operating temperature ranges.

Kemme [11] first performed a limited investigation to determine the performance limit of gravity-assisted sodium heat pipes. Somewhat later, Prenger and Kemme [12] performed extensive experiments on the entrainment limit for gravity-assisted heat pipes using various working fluids and proposed a dimensionless criterion, but the study lacked instrumentation to detect the onset of entrainment. In parallel with these heat pipe experiments, Matveev *et al.* [13] conducted a simple experiment to visualize the onset of entrain-

† Author to whom correspondence should be addressed.

NOMENCLATURE

A area of flow passage [m^2]
A_w wick cross-sectional area [m^2]
c_c bulk specific heat of the condenser [J kg^{-1} K^{-1}]
c_{p_c} specific heat of the coolant [J kg^{-1} K^{-1}]
d characteristic diameter [m]
d_1 wire spacing [m]
d_2 wire thickness [m]
$d_{h,w}$ hydraulic diameter of a wick pore [m]
D_h duct hydraulic diameter or vapor core diameter [m]
D_v dynamic pressure coefficient
F_l liquid frictional coefficient
F_v vapor frictional coefficient
h film thickness [m] or enthalpy [J kg^{-1}]
h_f flooding height [m]
h_t tilt height [m]
k_w wick thermal conductivity [W m^{-1} K^{-1}]
K permeability [m^2]
$\dot{m}_c$ coolant mass flow rate [kg s^{-1}]
$\dot{m}_E$ mass flow rate of entrainment [kg s^{-1}]
M_c bulk mass of the condenser [kg]
M_{ea} bulk mass of the evaporator plus adiabatic region [kg]
N_{ad} mesh number in the adiabatic region [m^{-1} or in.$^{-1}$]
N_b mesh number of the bottom wick [m^{-1} or in.$^{-1}$]
N_{vi} dimensionless viscosity number
P_l liquid pressure [Pa]
P_v vapor pressure [Pa]
$(\Delta P_c)_{pm}$ maximum permissible pressure [Pa]
$(\Delta P_c)_{max}$ pressure difference due to surface tension [Pa]
ΔP_l pressure drop in the liquid [Pa]
ΔP_v pressure drop in the vapor [Pa]
q_{ext} extra heat addition [W]
q_{cap} capillary limit [W]
r_c capillary radius [m]
r_i inner radius of a heat pipe [m]
$r_{h,l}$ hydraulic radius of liquid channel [m]
r_v vapor core radius [m]
Re duct Reynolds number of vapor flow
T_c coolant temperature or bulk mean temperature of the condenser [K or °C]
T_{ea} bulk mean temperature of the evaporator plus adiabatic region [K or °C]
ΔT_c coolant temperature rise [K or °C)
U mean vapor velocity [m s^{-1}]
U_{vc} critical mean velocity [m s^{-1}]
We Weber number.

Greek symbols
γ gas constant [J kg^{-1} K^{-1}]
λ wavelength [m]
λ_c critical wavelength [m]
μ viscosity of fluids [Pa s^{-1}]
ν kinematic viscosity of fluids [m^2 s^{-1}]
ρ density of fluids [kg m^{-3}]
σ surface tension of the liquid [N m^{-1}]
ψ tilt angle [rad].

Subscripts
a adiabatic region
ad adiabatic region
c critical values at the onset of instability or entrainment
cond conduction
dr dry-out
e entrainment limit or evaporator
ea evaporator plus adiabatic region
eva evaporator
E entrainment
l liquid
th thermal detection of entrainment
v vapor
vi visual detection of entrainment.

ment and to verify Cotter's instability criterion using an air–water test channel interrupted by screen mesh. This type of aerodynamic simulation was more intensively studied by Kim *et al.* [14] to simulate the effects of both the vapor velocity and wick dimensions on the entrainment phenomenon in heat pipes. From the results of the parametric study, the measured critical air velocities for fine meshes ($N \geqslant 40$) were found to be in good agreement with those predicted by the theoretical models [9, 15], but it was uncertain whether these models could be applied to operating heat pipes whose vapor velocity is not extremely high.

For the present investigation, a copper–water heat pipe was constructed from copper tubes and a rectangular copper duct. The entire length of the heat pipe was approximately 2.16 m, which was long enough to apply a maximum power of 7.3 kW prior to dry-out. Entrainment was detected by various methods and classified into representative types according to the relative position of the liquid interface to the wick structure and the operating condition. A high speed video camera and image analyzer were utilized to visualize and classify the various modes of entrainment.

The principal objective of the proposed research was to investigate the entrainment phenomena in capillary-driven heat pipes so that the entrainment limit for a given wick size and operating temperature

could be predicted more accurately during the design stage. Goals and tasks of the present investigation included (1) theoretical verification of the existence of entrainment using a computer model to determine the maximum heat transport, (2) entrainment characterization to identify and describe the entrainment configuration and generation mechanisms in an operating heat pipe using flow visualization techniques, (3) development of a dimensionless empirical correlation proposed to predict the entrainment limit as a function of both vapor temperature and physical dimensions and (4) comparison of these data with analytical or empirical models developed in previous studies.

SUMMARY OF PREVIOUS STUDIES

To review the various entrainment or critical velocity models in operating heat pipes, 12 previous models were examined to investigate individual trends and any disparities in the general tendency of the models. In order to organize the previous studies, the entrainment was categorized into two types based on the relative position of the liquid interface and the wicking structure, i.e. wave-induced entrainment and shear-induced entrainment, as shown in Table 1.

In the two groups of entrainment models, the wave-induced entrainment occurred when the wick structure was fully flooded. The instability criterion [3], the modified flooding correlation for non-wicked heat pipes [7] and the roll-wave model [6] can be included in this category. The shear-induced entrainment resulted from the shear forces induced by high velocity vapor flows when the wick structure was properly saturated. Several analytical models such as the Weber number criterion [10], the instability criterion [9] and the entrainment limit criterion derived from flooding correlations [7], etc. were investigated to predict the entrainment limit in wicked heat pipes.

The characteristic dimensions and significant thermodynamic properties involved in the criteria are also presented to assist in this comparison. For the characteristic dimensions, the shear-induced models are associated with smaller dimensions than the wave-induced models. In particular, Prenger [12] and Prenger and Kemme [16] show the smallest values for the twelve models studied. For the thermodynamic properties involved in the criteria, all the models were found to be related to the surface tension and vapor density, but the liquid viscosity can be seen in only the roll-wave model proposed by Ishii and Grolmes [6].

As shown in Table 1, 12 models (five models for the wave-induced entrainment and seven for the shear-induced entrainment) were examined to determine the individual trends and deviation from the general tendency of the overall models. For this purpose, critical Weber numbers were calculated for the chosen characteristic dimensions of the interface and the working fluid (water). A film thickness, h, of 4 mm was used as a characteristic dimension for the calculations of the wave-induced entrainment group, and the wire spacing for 40×40 copper mesh ($= 0.53$ mm according to McMaster–Carr (1991)) was utilized for that of the shear-induced entrainment group. Particularly, the hydraulic diameter, $d_{h,w}$, in the Weber number criterion of Chi [10] was assumed to be the wire spacing, d_l, of the mesh, and wire thickness was used for the characteristic dimension, δ, in the dimensionless correlations of Prenger and Kemme [16] and Prenger [12]. The hydraulic diameter of the vapor core D_h was assumed to be 15.2 and 19.2 mm for the wave- and shear-induced entrainment, respectively.

The critical Weber number is the Weber number corresponding to the onset of entrainment and is defined as the ratio of the inertia force to the surface tension force, i.e. the Weber number is expressed as $We = \rho_v U_v^2 L/\sigma$, where L is the characteristic dimension of the interface. For the entrainment limit models such as Tien and Chung [7] and Kemme [11], the critical vapor velocity can be estimated using an energy balance:

$$U_{vc} = \frac{q_e}{\rho_v A_v h_{fg}}. \quad (1)$$

In general, lower critical Weber numbers indicate that the onset of entrainment initiates at a lower vapor velocity for the given dimension and temperature. Since changes in the vapor temperature may cause the critical Weber number to vary due to property changes, the critical Weber numbers must be presented as a function of the vapor temperature. However, the effect of changes in liquid properties on entrainment cannot be well described by the Weber number itself. Thus, the viscosity number was introduced as $N_{vi} = \mu_l/\sqrt{(\rho_l \sigma \lambda_c/2\pi)}$ to describe the stability of the liquid as the vapor temperature changed.

In Fig. 1, the critical Weber number, We_{vc}, is plotted as a function of the viscosity number, N_{vi}, corresponding to the vapor (or saturation) temperature to show the individual trends of the various models. The solid and blank symbols are associated with the wave- and shear-induced models, respectively. Six models including Cotter [9] and Chi [10] show that the critical Weber number remains unchanged with decreases in the viscosity number. However, increasing trends are observed by two models, the instability model for the wave-induced entrainment [3] and the turbulent roll-wave model [6]. Alternatively, decreasing trends were indicated by the four models including Tien and Chung [7] and Prenger [12]. In addition, the overall trend of all the models indicates that the wave-induced entrainment models are associated with higher critical Weber numbers than those for the shear-induced entrainment models except for the transition model of Ishii and Grolmes [6]. This overall trend may be reasonable since the characteristic dimension for the wave-induced entrainment is generally larger than for the shear-induced entrainment in capillary-driven heat pipes, as indicated in Table

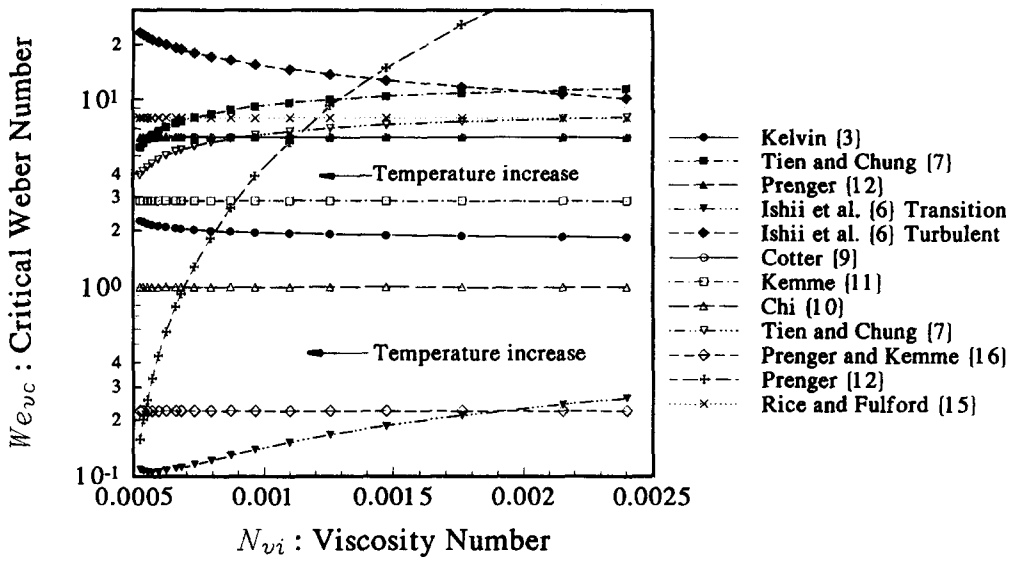

Fig. 1. The critical Weber number vs viscosity number for various entrainment models.

1. A characteristic dimension, approximately 4 times larger was used for the wave-induced entrainment in the present investigation.

The overall trend shows that the order of magnitude of the critical Weber number varies from 0.1 to 20, and individual trends are not consistent with respect to the vapor temperature change. Model comparisons between Ishii and Grolmes [6] and Prenger [12] (for the shear-induced model) show significant differences in the trends. In general, the critical Weber number tends to increase very rapidly with increases in the viscosity number for large values of the viscosity number, but the dependency diminishes as the viscosity number decreases, thereafter the Weber number approaches a limiting value according to Hinze [17]. In this sense, the theoretical shear-induced model presented by Prenger [12] seems to lack theoretical validity. This may be caused by the inappropriate geometry, i.e. the configuration of the interface shown in Fig. 1 is appropriate for the wave-induced entrainment, but not for the shear-induced entrainment. Also, the overall trend indicates that in most cases, the critical Weber number does not show significant variation except for $N_{vi} < 0.0007$ regardless of the large difference in the predicted values.

EXISTENCE OF ENTRAINMENT

In operating heat pipes, the existence of entrainment is often affected by other performance limitations, such as the capillary limit and boiling limit. Entrainment occurs only after the drag forces due to the high velocity of the vapor are large enough to tear liquid droplets off the liquid interface. Thus, the entrainment will not be reached if the heat transport prior to the onset of entrainment exceeds that of the other performance limits, i.e. the capillary limitation or the boiling limitation.

As noted by Busse and Kemme [8], another necessary condition for the existence of entrainment is that the wick be saturated with liquid. This implies that entrainment can occur at the wet point: however, the possibility of entrainment becomes less as the wet point is subjected to condensation. Thus, the inlet of the adiabatic region may be the most likely point for entrainment when flooded and subjected to high velocity vapor flow.

Because of these requirements, the present investigation first theoretically investigates the capillary and boiling limitations, and then compares these theoretical results with experimental data.

Capillary limitation

To determine the capillary limit (or dry-out limit), pressure drops in both the liquid and vapor channel were investigated. A one-dimensional vapor flow model from Chi [10] was utilized to predict the vapor pressure drop, while the momentum equation for the liquid flow was simplified and solved to calculate the liquid pressure drop using previous investigations for wick permeability.

(1) *Vapor pressure drop.* The vapor pressure gradient can be written in an alternative form [10]:

$$\frac{dP_v}{dx} = -F_v q - D_v \frac{dq^2}{dx} \tag{2}$$

where F_v and D_v are the frictional and the dynamic pressure coefficients, respectively, and are defined as

$$F_v = \frac{(f_v Re_v)\mu_v}{2r_{h,v}^2 A_v \rho_v h_{fg}} \tag{3}$$

$$D_v = \frac{\beta}{A_v^2 \rho_v h_{fg}^2}. \tag{4}$$

Also, the Reynolds and the Mach number are expressed in terms of q as

$$Re_v = \frac{2r_{h,v}q}{A_v\mu_v h_{fg}} \quad (5)$$

$$Ma_v = \frac{q}{A_v\rho_v h_{fg}\sqrt{\gamma_v R_v T_v}}. \quad (6)$$

If the Reynolds and the Mach number are less than 2300 and 0.2, respectively, f_vRe_v is equal to 16 (for circular passages) as is the case for laminar and incompressible flow and β is equal to 1.33. For flow with large Reynolds numbers ($Re_v > 2300$) and $Ma_v < 0.2$, β is very close to unity, and f_vRe_v is no longer a constant value, where f_v corresponds to the Fanning friction factor in incompressible turbulent vapor flows:

$$f_v = \frac{0.079}{Re_v^{0.25}}. \quad (7)$$

Thus, the frictional and dynamic pressure coefficient in equations (3) and (4), respectively, can be represented for incompressible turbulent vapor flow as

$$F_v = \frac{0.039\mu_v}{A_v r_{h,v}^2 \rho_v h_{fg}}\left(\frac{2r_{h,v}q}{A_v h_{fg}\mu_v}\right)^{3/4} \quad (8)$$

$$D_v = \frac{1}{\rho_v A_v^2 h_{fg}^2}. \quad (9)$$

(2) *Liquid pressure drop.* Also, the liquid pressure gradient can be written in the form [10]

$$\frac{dP_l}{dx} = -F_l q \pm \rho_l g \sin\psi \quad (10)$$

where F_l is a frictional coefficient for the liquid flow and is defined as [10]

$$F_l = \frac{\mu_l}{K_l A_w h_{fg}\rho_l}. \quad (11)$$

Here, K_l indicates the wick permeability, which represents a property of the wick structure [10].

(3) *Pressure balance in operating heat pipes.* The fundamental mechanism that governs heat pipe performance is a result of the difference in the capillary pressure across the liquid–vapor interface, which is equal to the pressure difference between the liquid and vapor phase at any given axial position. For a heat pipe to function properly, the net capillary pressure between the wet point (where $P_l = P_v$ in the condenser) and the beginning of the evaporator must be greater than the summation of all the pressure losses occurring throughout the liquid and vapor flow path. This can be expressed mathematically as

$$(\Delta P_c)_{max} \geqslant \Delta P_v + \Delta P_l + \Delta P\perp \quad (12)$$

where $\Delta P\perp$ is the normal hydrostatic pressure drop and defined as

$$\Delta P\perp = \rho_l g d_v \cos\psi. \quad (13)$$

Here, d_v and L_t are vapor core diameter and total length, respectively and $(\Delta P_c)_{max}$ is the maximum capillary pressure derived from the Laplace–Young equation. If the local capillary radius in the condenser is neglected, $(\Delta P_c)_{max}$ can be expressed a function of only the effective capillary radius of the evaporator wick ($r_{c,e}$) or

$$(\Delta P_c)_{max} = \frac{2\sigma}{r_{c,e}}. \quad (14)$$

For the heat pipe illustrated in Fig. 2, the summation of the first two terms on the right side of equation (12) can be determined by integrating the pressure gradients in the vapor and liquid phase, equations (2) and (10), respectively, from the wet point (at the end of the condenser) to the beginning of the evaporator:

$$\Delta P_v + \Delta P_l = \int_0^{L_t}\left(\frac{dP_v}{dx} - \frac{dP_l}{dx}\right)dx. \quad (15)$$

Substituting equations (2) and (10) into equation (15):

$$\Delta P_v + \Delta P_l = \int_0^{L_t}\left(F_v q - D_v\frac{dq^2}{dx} + F_l q + \rho_l g\sin\psi\right)dx. \quad (16)$$

The vapor frictional term, F_vq, becomes positive since the vapor is flowing opposite the direction of integration, as shown in Fig. 2. In addition, using D_v given in equation (4), the integration of the second term in equation (16) leads to zero since q is equal to zero at both ends of the heat pipe. Substituting equations (13)–(16) into equation (12), a relationship, referred to as the capillary limitation, can be obtained as

$$(\Delta P_c)_{pm} = \frac{2\sigma}{r_{c,e}} - \rho_l g d_v\cos\psi - \rho_l g L_t\sin\psi = \int_0^{L_t}(F_v + F_l)q\,dx \quad (17)$$

where $(\Delta P_c)_{pm}$ is referred to as the maximum permissible capillary pressure.

(4) *Calculation of the capillary limit.* If the vapor flow is assumed to be one-dimensional and laminar ($Re_v < 2300$), both F_v in equation (3) and F_l in equa-

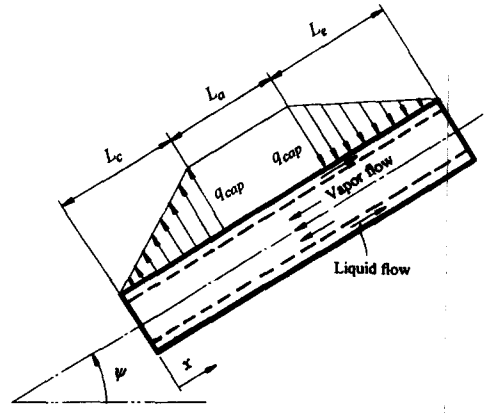

Fig. 2. Schematic illustration of an operating heat pipe with the maximum heat transport, q_{cap}.

tion (11) are constant. Thus equation (17) can be rewritten as

$$\int_0^{L_t} q\,dx = \frac{(\Delta P_c)_{pm}}{(F_v + F_l)}. \quad (18)$$

For the case of a uniform heat flux distribution along the evaporator and condenser sections, the right side of equation (18) can be integrated along the heat pipe as

$$\int_0^{L_t} q\,dx = (0.5L_c + L_a + 0.5L_e)q_{cap} = L_{eff}q_{cap} \quad (19)$$

where q_{cap} is the capillary limit and L_{eff} is the effective length of a heat pipe for the given length of the condenser, evaporator and adiabatic region. Hence, for the laminar vapor flow, the capillary limit, q_{cap}, can be explicitly determined from equations (18) and (19) as

$$q_{cap} = \frac{(\Delta P_c)_{pm}}{(F_v + F_l)L_{eff}}. \quad (20)$$

For one-dimensional turbulent flow, the capillary limit can no longer be determined explicitly since the vapor frictional coefficient, F_v in equation (8), is a function of q. Substituting equation (8) into equation (17) yields

$$(\Delta P_c)_{pm} = \frac{0.039\mu_v}{A_v r_{h,v}^2 \rho_v h_{fg}} \left(\frac{2r_{h,v}}{A_v h_{fg}\mu_v}\right)^{3/4} \times \int_0^{L_t} q^{7/4}\,dx + F_l \int_0^{L_t} q\,dx. \quad (21)$$

For a uniform heat flux condition in the evaporator and condenser, q is represented as a function of x:

$$q = q_{cap}\frac{x}{L_e} \quad \text{for} \quad 0 \leqslant x < L_e \quad (22)$$

$$q = q_{cap} \quad \text{for} \quad L_e \leqslant x < L_e + L_a \quad (23)$$

$$q = q_{cap}\frac{L_t - x}{L_c} \quad \text{for} \quad L_e + L_a \leqslant x \leqslant L_t. \quad (24)$$

Substituting equations (22)–(24) into equation (21) yields

$$(\Delta P_c)_{pm} = \frac{0.039\mu_v}{A_v r_{h,v}^2 \rho_v h_{fg}} \left(\frac{2r_{h,v}}{A_v h_{fg}\mu_v}\right)^{3/4} \left(\frac{11}{4}L_e + L_a + \frac{11}{4}L_c\right) q_{cap}^{7/4} + F_l q_{cap} L_{eff}. \quad (25)$$

Boiling limitation

If the radial heat flux of the heat pipe at the evaporator exceeds a critical value, vapor bubbles may be formed in the evaporator wick because the saturation vapor pressure corresponding to the wick–pipe interface temperature is higher than the local liquid pressure and is sufficient to cause nucleation [5, 10]. The bubbles may grow and become trapped in the wick, blocking the liquid return and resulting in evaporator dry-out. This phenomenon, referred to as the boiling limit, differs from the capillary limitation in that it depends on the radial heat flux at the evaporator as opposed to the axial heat flux.

Determination of the boiling limitation is based on homogeneous nucleation in a superheated liquid and heterogeneous nucleation and bubble growth from a heated surface. This involves two separate phenomena, i.e. bubble formation and the subsequent growth or collapse of the bubbles, respectively. By performing a pressure balance on any given bubble and using the Clasius–Clapeyron equation to relate the temperature and pressure, an expression for the heat flux beyond which bubble growth will occur was developed by Chi [10]. This expression, which is a function of the cavity size, r_n, and the fluid properties, can be written as

$$q_b = \frac{2\pi L_{eff} k_{eff} T_v}{\rho_v h_{fg} \ln(r_i/r_v)} \left(\frac{2\sigma}{r_n} - (\Delta P_c)_{max}\right). \quad (26)$$

Here k_{eff} is the effective thermal conductivity of the liquid–wick combination for the wrapped screen wick, given in Chi [10], and k_l and k_w are the thermal conductivity of the liquid and wick, respectively. In addition, r_i and r_n in equation (26) represent the inner radius of the heat pipe wall and the nucleation site radius, respectively. The nucleation site radius for conventional heat pipes can be assumed to be from 2.54×10^{-7} to 2.54×10^{-5} m according to Chi [10] and Dunn and Reay [18].

A model to predict the maximum performance

A computer model was developed based upon the theoretical background indicated in equations (20) and (25). For the present investigation, the Mach number, Ma_v, was assumed to be less than 0.2, and was verified by the computation. Basic assumptions for the computation are:

(1) The vapor channel is uniform in its cross-sectional area.

(2) The mesh number used in the evaporator is fixed, i.e. $N_{eva} = 100$ and the mesh in the adiabatic region varies ($N_{ad} = 40$, 80 and 200).

(3) N_{eva} ($= 100$) is used for the calculation of the maximum capillary pressure, $(\Delta P_c)_{max}$, if N_{ad} is not larger than 100.

(4) The wick permeability is estimated by Chi [10] for a composite wick (eight layers of bottom mesh ($N_b = 24$) and one layer of top mesh corresponding to N_{ad}) using an effective mesh number:

$$N_{eff} = \frac{4 \times N_b + N_{ad}}{5}. \quad (27)$$

EXPERIMENTAL APPARATUS

The heat pipe used in the current investigation was constructed from copper tubes and a rectangular copper duct as shown in Fig. 3. The entire length of the

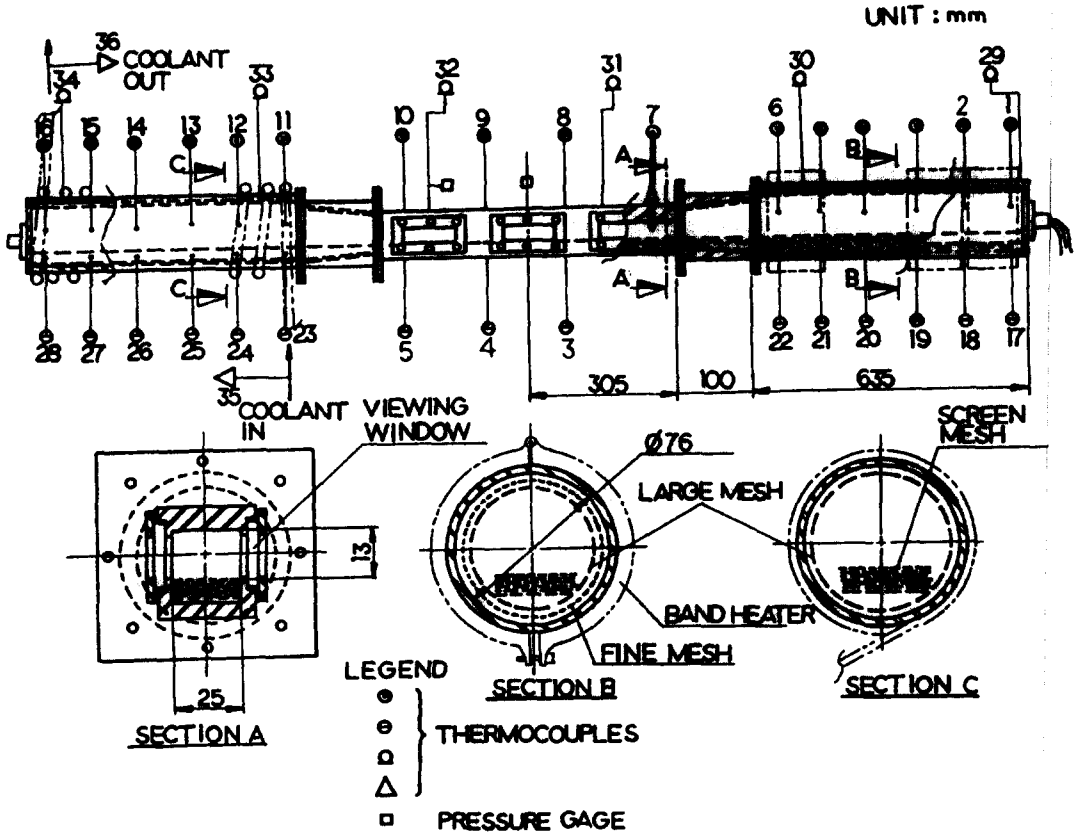

Fig. 3. Detailed configuration and dimensions of the test setup for heat pipe experiments.

heat pipe was approximately 2.16 m, long enough to apply a maximum power of 7.24 kW prior to dry-out. Both the evaporator and condenser were made of 0.76 m long copper tubes with an inner diameter of 76 mm. The adiabatic section was fabricated from a 0.64 m long rectangular copper duct. The vapor flow section of the adiabatic region is 25 mm wide and 15.7 mm high, and the liquid flow section is 25 mm wide and 12.7 mm high.

In the adiabatic region, six viewing windows were installed for flow visualization of the wicked interface. The copper mesh to be evaluated was inserted into a slit, under which 10 layers of copper mesh (mesh number 24) were installed to supply water to the evaporator. Detailed dimensions for the screen mesh are listed in McMaster–Carr (1991). To minimize peripheral dry-out of the evaporator, several layers of fine copper mesh (mesh number 100) were inserted between the inner wall of the evaporator and a large mesh (mesh number 4), which functions as a plate spring to maintain the gap as illustrated in Fig. 3.

Seven electric band heaters (maximum power = 7.24 kW) were installed on the outer surface of the evaporator to apply a uniform heat flux. The power to each heater was adjusted by means of individual variable power supplies. On the outer surface of the condenser, a 6 mm diameter copper coil was silver soldered circumferentially to reject the heat to the circulating coolant, as shown in Fig. 3. Two different temperatures of water, i.e. chilled water (7–10°C) and tap water (30–35°C) were used as coolants to adjust the operating vapor temperature.

Internal temperature variations of the liquid and vapor and the coolant temperature were monitored using 39 T-type thermocouples installed along the heat pipe as indicated in Fig. 3. Twenty-four thermocouples were installed along the heat pipe, 12 in the liquid and 12 in the vapor region of the evaporator and condenser, every 150 mm to investigate axial temperature variations. In the adiabatic region, four thin sheath-type thermocouples were installed to measure the vapor temperature and three for the liquid temperature. Six thermocouples for monitoring the wall temperatures were installed on the outer top surface every 0.36 m and two thin sheath-type thermocouples for measuring the temperature rise of the coolant were inserted into the coolant stream at the inlet and outlet to the coolant jacket. The temperature difference between the inlet and the outlet of the coolant was used to estimate the axial heat transport. In addition, two pressure transducers, P. T. No. 1 and P. T. No. 2 [pressure range: 0–0.4 MPa (abs)], were installed in the middle and at the end of the adiabatic region, respectively.

The 36 thermocouples (T. C. Nos 1–36) indicated in Fig. 3 were connected to the data logger. Three three-channel strip chart recorders were interfaced with thermocouples, T. C. Nos 3, 8, 11, 23 and 29,

and two pressure transducers, P. T. Nos 1 and 2, to investigate temporal changes in the operating conditions before and after entrainment.

For the flow visualization at the onset of entrainment, a high speed video camera (shutter speed: 1/4000 s) and an image analyzer with a strong back light (150 W flood lamp) were focused on the wicked interface in the inlet of the adiabatic region. To prevent condensation on the inner walls of the viewing windows, small stainless steel strip heaters were attached on the outer surface. Approximately, 20 W was supplied to each viewing window to eliminate wall condensation.

Two rotameters (recommended flow rate: 0.063–0.63 l s^{-1} and 0.032–0.32 l s^{-1}), and a water meter (totalizer) were serially connected to the outlet of the coolant circuit to accurately measure the coolant flow rate. In addition, a three-way valve was installed to evacuate and charge the heat pipe with working fluid. The flooding height in the adiabatic region was regulated by the on–off valve. A micro valve installed at the end of the condenser was used to remove non-condensable gases and control the operating conditions when the heat pipe was operating below atmospheric pressure.

EXPERIMENTAL PROCEDURE

Every run of the heat pipe experiment consisted of two processes, i.e. the startup process and the steady-state operation. The startup process was designed to avoid premature dry-out of the evaporator before the heat transport reached the entrainment limit, and to allow the heat pipe to be operated at a particular vapor temperature by balancing the heat input and the heat rejection. The facility used for charging is shown in Fig. 4 and the procedure was as follows: First, the heat pipe vacuum pressure was adjusted to about 0.01 torr by opening the micro valve at the end of the condenser. The heat pipe was then charged with purified water by switching the three-way valve. The liquid was allowed to flow into the heat pipe until the wick in the adiabatic region was properly saturated. After this, the coolant flowrate was set to a predetermined value (typically 0.126 l s^{-1}) and the band heaters were set to about 0.97 kW. For this typical procedure, the vapor temperature and pressure variations during the startup process are shown in Fig. 5.

Temperature and pressure variations during startup

The two vapor temperatures (T_{va} and T_{vc}) and vapor pressure (P_{vl}) were continuously recorded using a strip chart recorder. At the beginning of the experiment, the thermodynamic state of the working fluid in the evaporator was a compressed liquid. Prior to operation, the non-condensable gases which tended to accumulate in the condenser were evacuated using the micro valve shown in Fig. 4 so that the hot vapor in the evaporator can penetrate the condenser. The vapor temperature in the condenser inlet (T_{vc}) was

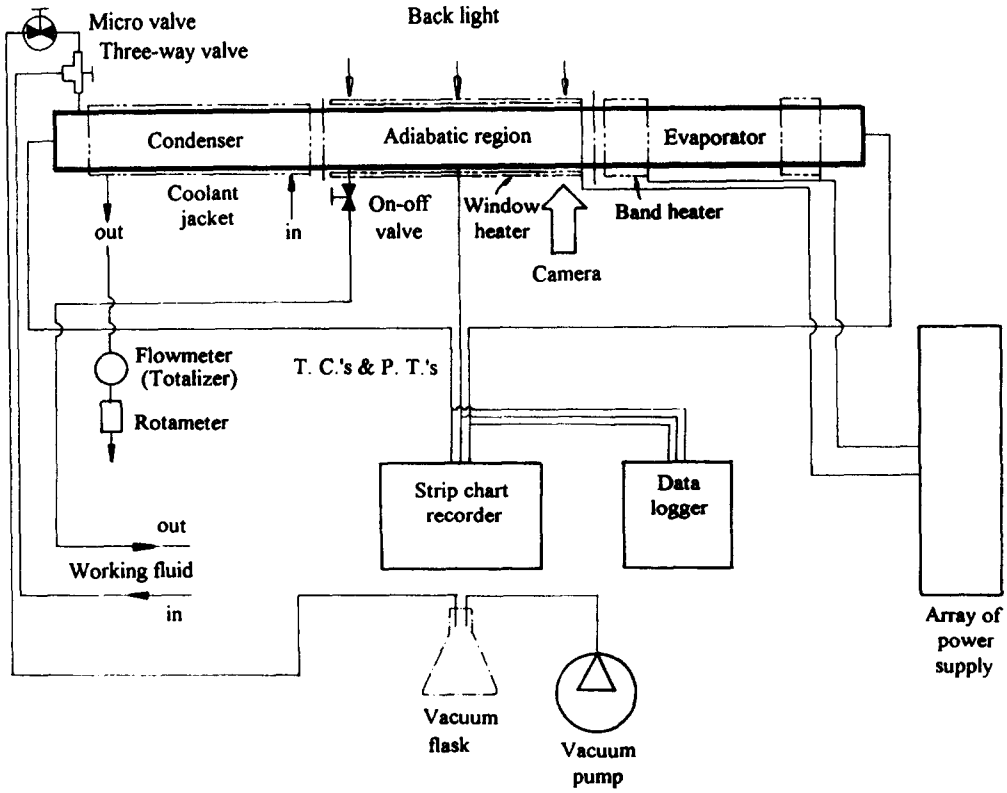

Fig. 4. Schematic diagram of the test setup for the heat pipe experiments.

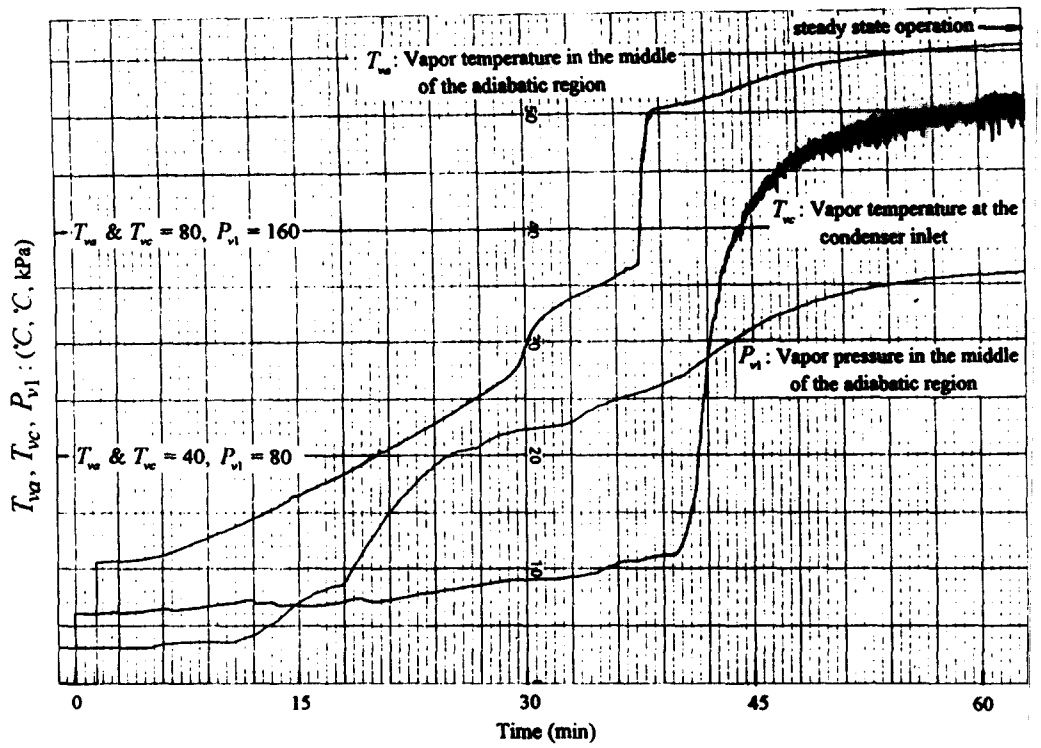

Fig. 5. Variations of the vapor temperature and pressure at the certain location prior to the steady-state operation.

much lower than T_{va} before removal of the noncondensable gases (shown by the sudden jumps in vapor temperatures at $t \approx 40$ min). Hereafter, the heat pipe operation gradually approach the steady-state conditions at $t \approx 60$ min.

As T_{va} and T_{vc} approached 110 and 100°C, respectively, the heat pipe began to operate in a steady-state mode and different steady-state conditions were obtained by increasing the heat input. With stepwise increases in heat input, the heat transport and vapor temperature (T_{va}) finally reached the range where the entrainment limit was to be measured. Once the vapor pressure (P_{vl}) becomes larger than the atmospheric pressure and the hot vapor fully penetrates the condenser region, the only way to control the vapor temperature (T_{va}) and corresponding heat transport is by varying the heat input. However, the micro valve was sometimes used to purge the noncondensable gases at operating vapor temperatures less than 70°C.

Measurement of entrainment limit

The heat transport at the onset of entrainment was calculated by measuring the temperature difference (ΔT_c) of the coolant flow between the inlet and outlet of the coolant circuit. However, the temperature rise may be affected not only by the convective heat transport, but also by the other heat transfer terms illustrated in Fig. 6. For control volume B in the condenser, the energy and mass balance equations for a steady state are

$$M_c c_c \frac{dT_c}{dt} = \dot{m}_v h_v - \dot{m}_l h_l + \dot{m}_E h_l + q_{cond} - q_{out} = 0 \quad (28)$$

$$\frac{dM_c}{dt} = \dot{m}_v - \dot{m}_l + \dot{m}_E = 0. \quad (29)$$

The steady-state energy equation for control volume A comprising the evaporator and adiabatic region becomes

$$M_{ea} c_{ea} \frac{dT_{ea}}{dt} = q_{in} + q_{ext} - q_{loss} - q_{cond} - \dot{m}_v h_v + \dot{m}_l h_l - \dot{m}_E h_l = 0. \quad (30)$$

The global energy equation for the heat pipe including both control volumes can be expressed as

$$q_{in} + q_{ext} = q_{loss} + q_{out}. \quad (31)$$

From either equations (28) or (30), a simplified energy balance can be derived using equations (29) and (31) if $\dot{m}_E$ is nearly zero:

$$q_{out} = q_{cond} + \rho_v A_v U_v h_{fg} = \dot{m}_c c_{p_c} \Delta T_c. \quad (32)$$

The conductive heat transfer term, q_{cond}, can be determined experimentally from the plots that show variations of the heat rejection, q_{out}, with respect to time. The heat rejection was observed to very slowly increase and remain constant (less than 0.2 kW in most cases) until the hot vapor flow reached the con-

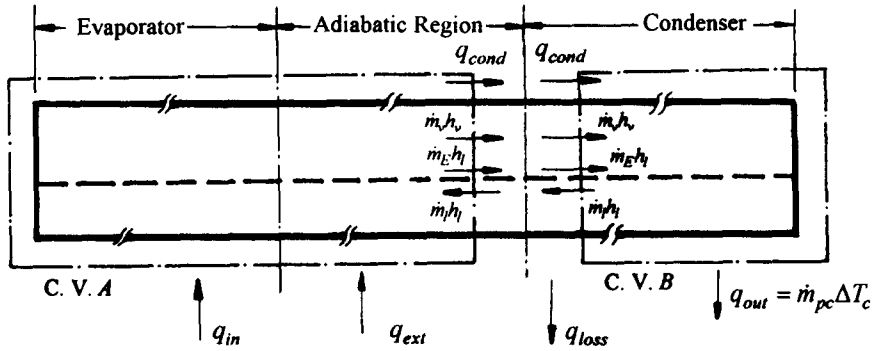

Fig. 6. Schematic illustration of various heat transfer terms in operating heat pipes.

denser. This is probably due to the fact that the heat rejection sensed by the coolant is negligible and the conductive heat transfer, q_{cond}, is dominant. In addition, the axial temperature gradient indicated by the difference in the average radial wall temperature between the evaporator and condenser should be at a maximum just before the vapor temperature at the condenser inlet (T. C. No. 23) starts to increase. This is reasonable since the mean radial wall temperature and the mean bulk temperature in the condenser tend to increase abruptly as the hot vapor starts to condense on the inner wall and interface. Instead, the evaporator wall temperature increases slowly unless the heat pipe is subjected to the dry-out limit. For the present investigation, the conductive heat transfer, q_{cond}, was neglected since $q_{cond} \ll \rho_v A_v U_v h_{fg}$.

In addition, if the heat loss from the viewing windows is assumed to be approximately equal to the heat addition ($q_{ext} \approx 0.2$ kW) from the window heaters and back lights, the effective heat transport contributed by the vapor flow (or entrainment limit), q_e at the onset of entrainment could be determined from experimental data for ΔT_c, as

$$q_e = \rho_v A_v U_{vc} h_{fg} = \dot{m}_c c_{p_c} \Delta T_c \qquad (33)$$

where c_{p_c} ($= 4.18$ kJ kg^{-1} K^{-1}) is the specific heat for the coolant, and A_v and U_{vc} represent the cross-sectional area for the vapor flow and the critical vapor velocity at the moment of entrainment.

CHARACTERIZATION AND DETECTION OF ENTRAINMENT

Before examining the thermal detection of the entrainment for different initial flooding and tilt heights, it is necessary to characterize the modes of entrainment in heat pipe experiments. Three major modes of entrainment were observed. These were (1) wave-induced entrainment, (2) pulsating entrainment and (3) intermediate entrainment.

Wave-induced entrainment. This type of entrainment typically results from roll-waves, which occur when the wick is fully flooded and subjected to increased air–vapor velocity. It was frequently observed in the steam-water experiments when the heat pipe was highly overcharged, but rarely in the air–water experiments since the wick was not normally maintained in a fully flooded condition. When the wick is flooded, roll-waves are established at the interface as shown in Fig. 7(a). The stability of this wavy surface may be affected by the interaction of three major forces, surface tension and gravitational forces, which tend to stabilize the interface and the viscous drag forces which tend to destabilize it. At the leeward side of the surface, air–vapor pressure tends to be lowest due to the swirling vortices induced by the boundary separation [19–21]. This may cause pressure asymmetry with respect to the wave crest. As a result, liquid bulges are formed and become detached by the air–vapor stream.

Pulsation entrainment. This is a mixed mode of wave-induced and intermediate entrainment and occurs when the wick is fully flooded and is subjected to a higher vapor velocity than that of wave-induced

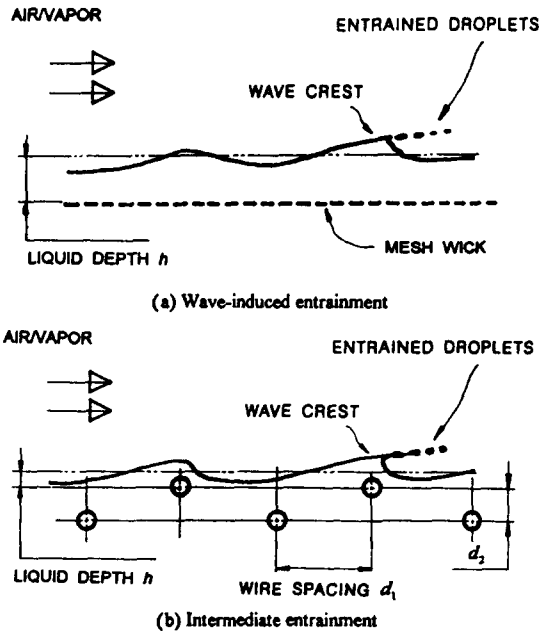

Fig. 7. Various entrainment modes observed in the heat pipe experiment; (a) wave-induced entrainment and (b) intermediate entrainment.

entrainment. The liquid is entrained as a form of periodic bursting caused by the interaction of surface waves and the shear force developed at the interface. The wave-induced entrainment becomes suppressed as the heat transport increases, but this mode lasts until the intermediate mode appears.

Intermediate entrainment. This type of entrainment was the most frequently observed shear-induced entrainment in steam–water experiments and occurs when the capillary-wick is covered with a relatively thin liquid film, whose depth is assumed to be so small that short waves propagate in the form of traveling waves as shown in Fig. 7(b). The thin liquid film is bounded by a fixed wicking structure and a free surface. Traveling waves (large disturbances) of relatively long wave length are formed due to the hydrodynamic instability of the liquid and grow unstable, when the phase velocity is larger than the interfacial liquid velocity [22]. Entrainment is observed as a form of periodic splashes induced by the shearing forces applied to the large disturbances.

Thermal detection of the intermediate entrainment

Entrainment limits corresponding to the intermediate mode were measured as functions of both the mesh number and the operating vapor temperature. For this parametric study, heat pipe experiments with both zero tilt and no initial flooding (i.e. $h_f = h_t = 0$) were performed for three different mesh sizes, $N_{ad} = 40, 80, 200$. In addition, chilled water ($T_{ci} = 8$–$10°C$) was used as a coolant for most cases and the coolant flowrate was varied from 0.025 to 0.25 l s^{-1} to control the vapor temperature. The coolant temperature was also changed by using tap water ($T_{ci} = 30$–$35°C$) to obtain higher vapor temperatures. Temperature fluctuations with and without the intermediate entrainment are compared in Fig. 8 under the typical operating conditions.

In addition to visual detection using the high speed video camera and the image analyzer, a new technique based upon pressure and temperature fluctuations in a saturated two-phase system was introduced to thermodynamically detect the onset of intermediate entrainment. Four thermocouples (Nos 3, 8, 11 and 23) in the adiabatic section (shown in Fig. 3) were used to continuously measure temperature fluctuations using strip chart recorders. For the case of no entrainment, there is no significant fluctuation in either T_{va} or T_{la} when compared with the entrainment case. If entrainment occurs near the inlet of the adiabatic region, the downstream local vapor pressure will tend to decrease. As a result, the local saturation vapor temperature detected by T. C. Nos 8 and 11 will also tend to decrease simultaneously, as shown in Fig. 8. Fluctuation of the liquid temperature (T. C. No. 3) in the middle of the adiabatic region implies not only a change in the corresponding saturation vapor temperature following entrainment but also penetration of the colder liquid into the middle of the adiabatic region due to both the capillary suction of the receded wick and the hydrostatic head developed by the waves in the condenser.

RESULTS AND DISCUSSION

The results obtained in this investigation include: (1) theoretical analysis of the effects of the heat pipe

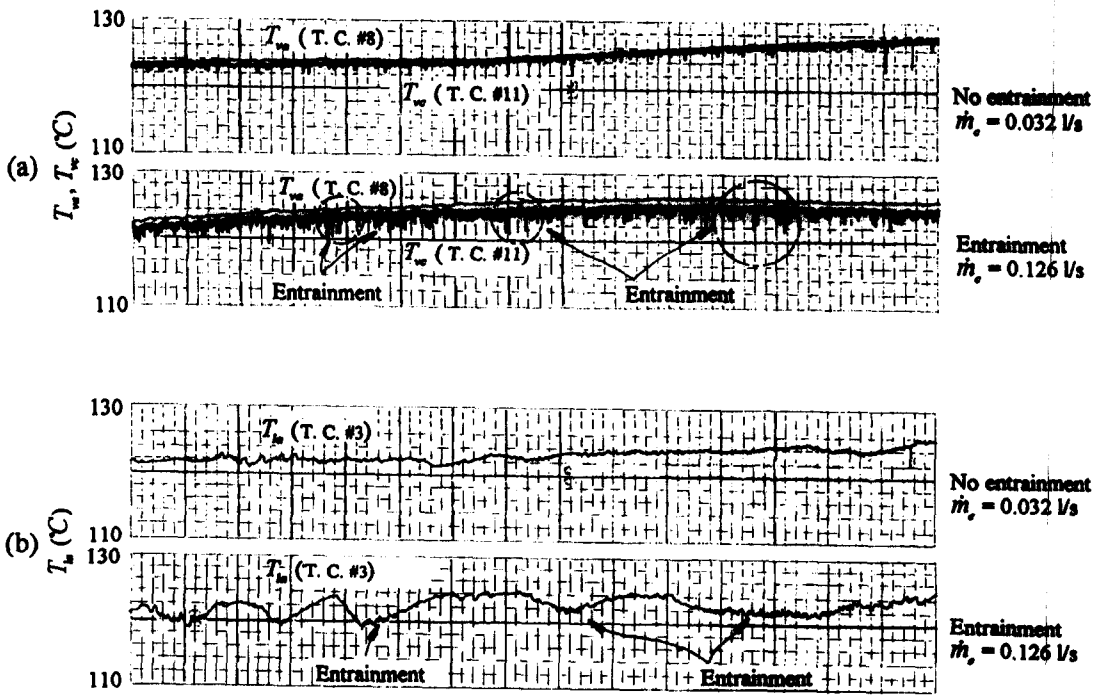

Fig. 8. Comparison of temperature variations for with and without entrainment; (a) T_{va} and T_{vc} vs time, (b) T_{la} vs time – $T_{ci} = 8$–10 (°C), $N_{ad} = 40$, $h_f = h_t = 0$, $q = 5.0$–5.7 (kW), paper feed rate = 1 cm min^{-1}.

geometry and operating condition of the maximum performance determined by the computer model to verify existence of entrainment and (2) physical interpretation of the behavior of the entrainment limit with variations in both vapor temperature and mesh number and derivation of a dimensionless empirical correlation corresponding to the experimental data.

Prediction of the maximum performance using the computer model

Using the computer model, a preliminary calculation was performed to determine an optimum vapor channel diameter for a particular mesh number ($N_{ad} = 40$) and saturation vapor temperature ($T_v = 102°C$), since the vapor channel diameter of the heat pipe in Fig. 3 is not axially uniform. The result of the preliminary calculation showed that the capillary limit was found to have a maximum at $D_h \approx 19$ mm, which is nearly the same as the hydraulic diameter of the vapor channel in the adiabatic region.

Three performance limits, q_{cap}, q_e and q_b, are presented in Fig. 9 as a function of the vapor temperature for three different mesh numbers, $N_{ad} = 40$, 80 and 200. As noted earlier, q_{cap} for $T_v > 60°C$ tends to decrease with increases in the mesh number, but shows increases in the predicted value as the mesh number becomes larger than 80 since the contribution of $(\Delta P_c)_{max}$ to q_{cap} becomes more significant. However, q_{cap} for $N_{ad} = 200$ becomes larger than for $N_{ad} = 40$ if T_v becomes less than 60°C since $(\Delta P_c)_{max}$ becomes more dominant as the surface tension force, σ, increases. The boiling limit with $r_n = 2.54 \times 10^{-7}$ (m) is independent of the mesh number in the adiabatic region and tends to decrease with increases in the vapor temperature since ρ_v in equation (26) rapidly increases but σ decreases with T_v. However, as shown in Fig. 9, the capillary limit, q_{cap}, was found to be more important than the boiling limit unless the vapor temperature is larger than 160°C. Based upon this observation, the dry-out limits obtained by the heat pipe experiment are less likely to be associated with the boiling limit than the capillary limit since the measured vapor temperatures are below 140°C.

The capillary limit is also compared with the entrainment limits predicted by Ishii and Grolmes [6] and Cotter [9] and shows an intermediate value of the two limits. Besides the observation that the entrainment is larger than q_{cap}, it can be deduced that the entrainment mode described by Cotter [9] cannot exist in heat pipe experiments.

Experimental results

The critical heat transport at the onset of the intermediate entrainment was measured for different mesh sizes by varying the coolant flow rate. The heat transport was calculated from equation (33) where the coolant temperature rise, ΔT_c, was measured by thermocouples, T. C. Nos 35 and 36. The mean vapor temperatures in the adiabatic region were obtained by averaging the four vapor temperatures measured by T. C. Nos 8–10.

Complete data sets of the heat pipe experiment for the case of zero tilt and no initial flooding are presented in Fig. 10. The heat transport at the onset of entrainment and dry-out are presented as a function of vapor temperature for different mesh numbers. General trends show that the entrainment and dry-out limit tend to increase as the vapor temperature increases, which is consistent with the results calculated from the computer model as indicated in Fig. 9. This trend can be explained by the significant increase in the vapor density as temperature increases, i.e. the vapor density at $T_v = 60°C$ is approximately 18 times larger than that at $T_v = 140°C$. More heat is required for a liquid at higher temperatures to vaporize at the same rate.

To verify the existence of the intermediate entrainment in the present investigation, the complete data set was compared with both the theoretical capillary limit obtained by assuming the hydrostatic head, h_s,

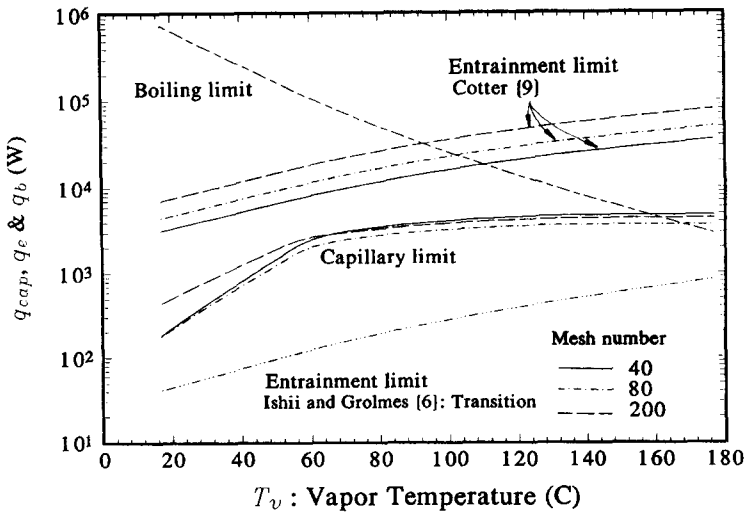

Fig. 9. Prediction of the capillary limit as functions of both vapor temperature and mesh size.

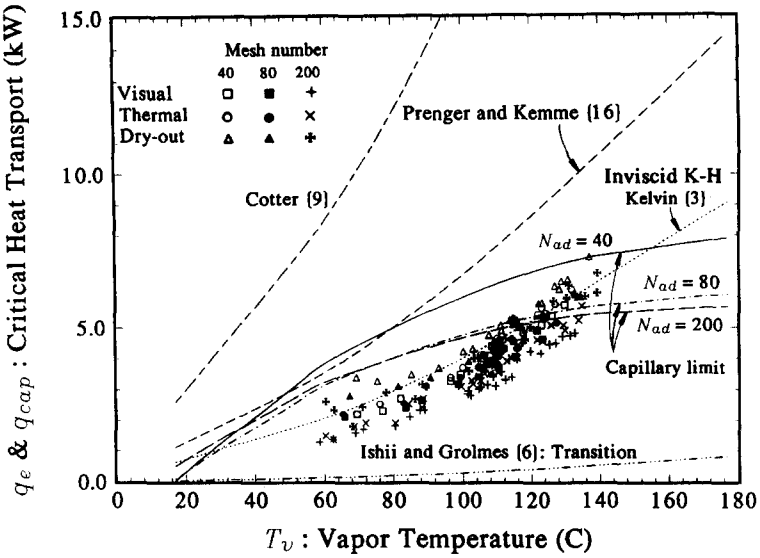

Fig. 10. Comparison of experimental data with theoretical predictions.

is equal to 40 mm. The effect of the hydrostatic head, h_s, on the increase of q_{cap} is theoretically the same as the favorable tilt height whose effect can be explicitly determined, but the effect of h_s is not. However, for the heat pipe experiment, the contribution of h_s on q_{cap} is supposed to gradually increase with increases in the heat transport. An approximate range of h_s was presumed to be 0–40 mm, which was indirectly calculated by multiplying a proportionality factor to the flooding height measured (3–4 mm) at the inlet of the condenser when the heat transport approaches that of the dry-out limit.

As shown in Fig. 10, for each mesh, most of the dry-out data are below the theoretical capillary except the case where $N_{ad} = 200$ and $T_v > 120$°C. In both Cotter [9] and Prenger and Kemme [16], the entrainment limit, q_e, was calculated for the case that $N_{ad} = 40$ and both models were developed based on the shear-induced mode. Instead, both the inviscid K–H [3] and the transition roll-wave model [6] are supposed to predict the wave-induced entrainment so that the entrainment limit, q_e, was calculated by assuming the liquid interface was about 4 mm above the mesh wick. Comparison of the experimental data with these four models shows that all of the experimental data are below the two models designed to predict the shear-induced entrainment, which is acceptable because the experimental data were measured based on the intermediate entrainment. Also, the experimental data are above the transition roll-wave model but slightly below the inviscid K–H model. This implies that the inviscid K–H model tends to overestimate q_e corresponding to the wave-induced entrainment, so it is not appropriate to predict q_e for the intermediate entrainment.

To investigate the effect of vapor temperature on the stability of the liquid interface, the critical Weber number, We_{vc}, and viscosity number, N_{vi}, are introduced and defined as

$$We_{vc} = \frac{\rho_v U_{vc}^2 \lambda_c}{\sigma} \quad N_{vi} = \frac{\mu_l}{\sqrt{\rho_l \sigma \lambda_c / 2\pi}} \tag{34}$$

where λ_c is the critical wavelength derived from the Rayleigh–Taylor instability [4] and N_{vi} represents the stability of a liquid interface. The critical vapor velocity, U_{vc}, corresponding to the measured entrainment limit was calculated from equation (1). Using these two parameters, the entrainment limit data shown in Fig. 10 can be represented as shown in Fig. 11, in which We_{vc} is presented as a function of N_{vi} for the three different meshes. The critical Weber number tends to increase slightly as N_{vi} decreases (or T_v increases). This implies that entrainment is supposed to be retarded as T_v increases even though the liquid becomes more unstable.

The critical Weber number tends to decrease as the mesh number increases. This is consistent with the trend of the entrainment limit data indicated in Fig. 10 but is quite different from those of Cotter [9] shown in Fig. 9. This discrepancy in the trends may be caused by the difference in entrainment modes involved in both experimental data and theoretical results. The present experimental data were obtained by measuring heat transport at the onset of intermediate entrainment. Instead, Cotter's model may be a more appropriate one to predict the onset of the shear-induced entrainment observed in air–water experiments [14]. For the shear-induced entrainment, larger heat transports or vapor velocities are required to entrain liquids. However, for the intermediate entrainment, the onset heat transport or vapor velocity

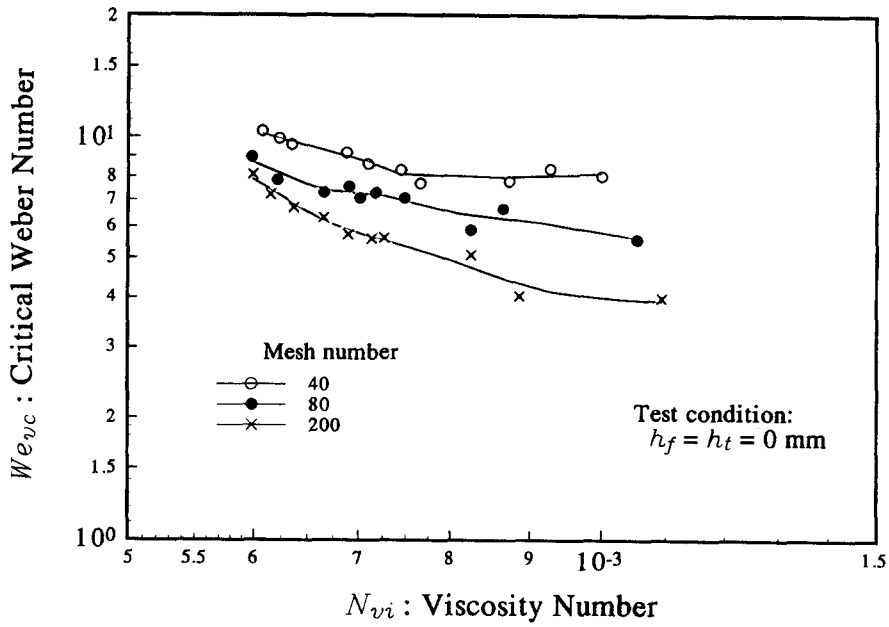

Fig. 11. Critical Weber number vs viscosity number for different mesh sizes.

becomes lower as waves formed on the thin liquid film are less retarded by the wick structure as the mesh number increases.

Dimensionless correlation

If mesh dimensions are also taken into consideration for this parametric study, the critical Weber number can be expressed by three independent terms, N_{vi}, λ_c/d_1 and D_h/d_2. This results in a functional relationship of the form as

$$We_{vc} = c_1 N_{vi}^{x} \left(\frac{\lambda_c}{d_1}\right)^{y} \left(\frac{D_h}{d_2}\right)^{z}. \quad (35)$$

If the three sets of experimental data shown in Fig. 11 are substituted into this equation, the unknown constant and exponents can be determined using a least-squares method. As a result, the dimensionless correlation for the critical Weber number can be expressed as

$$We_{vc} = 10^{-1.163} N_{vi}^{-0.744} \left(\frac{\lambda_c}{d_1}\right)^{-0.509} \left(\frac{D_h}{d_2}\right)^{0.276}. \quad (36)$$

For a fixed value of N_{vi}, We_{vc} tends to decrease as λ_c/d_1 increases (or mesh number increases), which is a physically reasonable trend. However, We_{vc} shows a contradictory trend for D_h/d_2 because We_{vc} tends to increase with increases in the term D_h/d_2 (or increases in the mesh number). However, the individual effects of the dimensionless mesh dimensions, λ_c/d_1 and D_h/d_2, may not be consistent with the trends of the experimental data shown in Fig. 12. If the combined effect of the two terms is taken into consideration, We_{vc} must decrease as d_2 decreases since the corresponding larger decrease associated with the term $(\lambda_c/d_1)^{-0.509}$ overrides the increase of $(D_h/d_2)^{0.276}$.

The measured critical Weber number, We_{vc}^{m}, is normalized by the critical Weber number predicted from equation (36), We_{vc}^{p}, and is presented in Fig. 12 as a function of N_{vi}. The experimental data and empirical correlation show fairly good agreement and are within $\pm 20\%$.

SUMMARY AND CONCLUSIONS

Entrainment phenomenon in capillary-driven heat pipes has been investigated experimentally and analytically to identify and better understand the parameters that govern the entrainment of liquid in operating heat pipes. For this purpose, a heat pipe experiment was conducted using a specially designed high power heat pipe with observation windows in the adiabatic section.

The heat pipe experiment was first designed to verify the existence of the various modes of entrainment and second, to measure the corresponding entrainment limits. Parametric studies were performed using the computer model developed based on equation (20) and (25) to investigate the effects of the mesh number in the adiabatic region (N_{ad}) and vapor temperature (T_v). Three performance limits, q_{cap}, q_e and q_b are presented in Fig. 9 as a function of the vapor temperature for three different mesh numbers, $N_{ad} = 40$, 80 and 200. Both the entrainment limit [9] and the boiling limit [10] were found to be larger than the capillary limit, which implies that the maximum performance of the heat pipe may be more likely to be limited by the capillary limit. Also, q_{cap} for $T_v > 60°C$

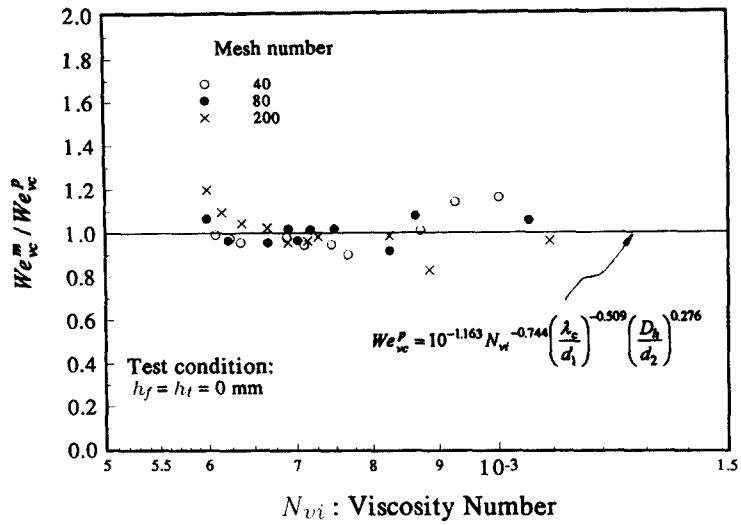

Fig. 12. Comparison of experimental data with those predicted by the empirical correlation.

tends to decrease with increases in the mesh number but shows increases in the predicted value as the mesh number becomes larger than 80 since the contribution of $(\Delta P_c)_{max}$ to q_{cap} becomes more significant.

Entrainment in the heat pipe experiment was classified into three major modes, i.e., wave-induced, pulsating and intermediate modes, according to not only the flow visualization experiment, but also the temperature fluctuation patterns at the onset of the individual entrainment modes.

As shown in Fig. 10, comparison of entrainment limit data with four models shows that all of the experimental data are below the two models [9, 16] designed to predict the shear-induced entrainment and above the transition roll-wave model [6], which predicts the wave-induced entrainment. This appears reasonable since the experimental data were measured based upon the intermediate entrainment.

As shown in Fig. 11, trends of the critical Weber number versus mesh number are quite different from those of the aerodynamic simulation investigated by Kim *et al.* [14]. The critical air velocity was found to increase with increases in the mesh number (i.e. the critical Weber number increases as the mesh number increases), while the critical Weber number in Fig. 11 shows the opposite trend. This discrepancy in the trends may be caused by the difference in entrainment modes at which both critical velocities are determined. The preceding analysis indicates that results of the air–water experiment, which are supposed to accurately predict the onset of the shear-induced entrainment like Cotter [9], may not be an accurate method of determining the critical vapor velocity or the entrainment limit of capillary-driven heat pipes.

To investigate the stability of the liquid interface, the experimental data were presented in terms of the critical Weber number based on λ_c vs the viscosity number. Results shown in Fig. 11 indicate that We_{vc} tends to increase slightly with decreases in N_{vi} similar to what was observed in Fig. 1. Also, a dimensionless correlation for the critical Weber number was developed using the experimental data shown in Fig. 12:

$$We_{vc} = 10^{-1.163} N_{vi}^{-0.744} \left(\frac{\lambda_c}{d_1}\right)^{-0.509} \left(\frac{D_h}{d_2}\right)^{0.276}.$$

This correlation was found to approximate the experimental data within $\pm 20\%$.

REFERENCES

1. M. N. Ivanovskii, V. P. Sorokin and I. V. Yagodkin, *The Physical Principles of Heat Pipe*, pp. 107–115. Clarendon Press, Oxford (1982).
2. G. P. Peterson and B. Bage, Entrainment limitations in thermosyphons and heat pipes, *ASME J. Energy Resour. Technol.* **113**(3), 147–154 (1991).
3. Kelvin (Edited by W. Thomson), On the influence of wind, *Phil. Mag.* **42**(281), 368–377 (1871).
4. P. G. Drazin and W. H. Reid, *Hydrodynamic Stability*, pp. 14–22. Cambridge University Press, Cambridge, U.K. (1981).
5. V. P. Carey, *Liquid–Vapor Phase Change Phenomena*, pp. 90–98. Hemisphere, Washington, DC (1992).
6. M. Ishii and M. A. Grolmes, Inception criteria for droplet entrainment in two-phase concurrent film flow, *A.I.Ch.E. Jl* **21**, 308–318 (1975).
7. C. L. Tien and K. S. Chung, Entrainment limits in heat pipes, *AIAA J.* **17**(6), 230–238 (1979).
8. C. A. Busse and J. E. Kemme, Dry-out phenomena in gravity-assisted heat pipes with capillary flow, *Int. J. Heat Mass Transfer* **23**, 634–654 (1980).
9. T. P. Cotter, Heat pipe startup dynamics, *Proceedings of the SAE Thermionic Conversion Specialist Conference*, pp. 344–347. Palo Alto, California (1967).
10. S. W. Chi, *Heat Pipe Theory and Practice*, pp. 33–95. Hemisphere, Washington, DC (1976).
11. J. E. Kemme, Vapor flow consideration in conventional and gravity assisted heat pipes, *Proceedings of the 2nd International Heat Pipe Conference*, pp. 11–21. Bologna, Italy (1976).

12. F. C. Prenger, Performance limits of gravity-assisted heat pipes, *Proceedings of the 5th International Heat Pipe Conference*, pp. 137–146. Tsukuba, Japan (1984).
13. V. M. Matveev, Y. N. Filippov, V. I. Dyuzhev and E. V. Okhapkin, Breakaway of a liquid by a gas stream at an interface containing grid, *J. Engng Phys.* **33**(3), 1008–1012 (1977).
14. B. H. Kim, G. P. Peterson and K. D. Kihm, Analytical and experimental investigation of entrainment in capillary-pumped wicking structures, *Trans. ASME J. Energy Resour. Technol.* **115,** 278–286 (1993).
15. G. Rice and D. Fulford, Influence of a fine mesh screen on entrainment in heat pipes, *Proceedings of the 6th International Heat Pipe Conference*, pp. 168–172. Grenoble, France (1987).
16. F. C. Prenger and J. E. Kemme, Performance limits of gravity-assisted heat pipes with simple wick structures, *Proceedings of the 4th International Heat Pipe Conference*, pp. 137–146. London, U.K. (1981).
17. J. O. Hinze, Fundamentals of the hydrodynamic mechanism of splitting in dispersion process, *A.I.Ch.E. Jl* **21,** 289–295 (1955).
18. P. D. Dunn and D. A. Reay, *Heat Pipes*, pp. 23–85. Pergamon Press, Oxford (1982).
19. M. L. Banner and W. K. Melville, On the separation of air flow over water waves, *J. Fluid Mech.* **77,** 825–842 (1976).
20. H. Jeffreys, On the formation of water waves by wind, *Proc. R. Soc. Lond.* **107,** 189–206 (1925).
21. M. J. Lighthill, Physical interpretation of the mathematical theory of wave generation by wind, *J. Fluid Mech.* **14,** 385–398 (1962).
22. J. W. Miles, On the generation of surface waves by turbulent shear flows, *J. Fluid Mech.* **7,** 469–478 (1959).